In situ optical emission study on the role of C$_2$ in the synthesis of single-walled carbon nanotubes

David Edmond Motaung,[1,2] Mathew Kisten Moodley,[1,3,a)] E. Manikandan,[1] and Neil J. Coville[3,4,b)]

[1]*National Centre for Nano-Structured Materials, Council for Scientific and Industrial Research, P. O. Box 395, Pretoria 0001, South Africa*
[2]*Department of Physics, University of the Western Cape, Private Bag X17, Bellville, 7535, South Africa*
[3]*School of Physics, University of the Witwatersrand, Private Bag 3, Johannesburg, 2050, South Africa*
[4]*DST/NRF Center of Excellence in Strong Materials and Molecular Sciences Institute, School of Chemistry, University of the Witwatersrand, Private Bag 3, Johannesburg, 2020, South Africa*

In situ optical emission spectroscopy was used to study the temporal and spatial behavior of laser induced plasmas in the laser-furnace synthesis of single-walled carbon nanotubes (SWCNTs). A graphite composite target located within a sealed quartz tube with a chemical stoichiometric composition of 95:4:1 at. wt % of carbon, yttrium, and nickel, respectively, was ablated by a Q-switched Nd:YAG laser delivering colinear, focused laser pulses of 1064 and 532 nm temporarily separated by 20 ns. The ablation process was done at a furnace temperature of 1273 K in a flow of argon gas at either 150 or 200 SCCM (SCCM denotes cubic centimeter per minute at STP). The pressure was varied (100, 400, and 600 Torr) for each gas flow setting. The temporal and spatial behavior of the emission intensity associated with C$_2$ Swan bands ($d\,{}^3\Pi_g - a\,{}^3\Pi_u$) was investigated and found to be influenced by the pressure and flow rate of the argon gas. At conditions optimal to SWCNT production, a sharp drop in C$_2$ intensity followed by a rise in C$_2$ intensity was observed. The temporal and spatial behavior of the electron density was determined by the Stark broadening profile of the CII emission peak at 283.7 nm and was found to decrease with the adiabatic expansion of the plume. We propose that the sharp drop in C$_2$ intensity and the rise in electron density and electron temperature observed in this study are due to the accompanying rapid nucleation and growth of SWCNTs. © *2010 American Institute of Physics*. [doi:10.1063/1.3311563]

I. INTRODUCTION

Single-walled carbon nanotubes (SWCNTs) are unique one-dimensional nanostructure with extraordinary electronic, thermal, optical, and mechanical properties.[1] These properties make SWCNTs suitable materials for a wide range of advanced technological applications.[2–4] While the application of SWCNTs have been demonstrated on a laboratory scale, these have yet to make it to the mass market because of reliability issues related to the lack of control of experimental parameters required to synthesize SWCNTs. Recently it has been demonstrated that density gradient ultracentrifugation[5] is a viable method to separate various SWCNT species. Nevertheless, it is still desirable for experimentalists to have some control over the formation of SWCNTs so that reliable electronic devices based on SWCNTs can become economically feasible. As a result, there is a continued effort by the international community to study growth mechanisms and experimental parameters for the controlled synthesis of carbon nanotubes. There are many methods for synthesizing carbon nanotubes, however, the most common methods are the arc-discharge,[6] chemical vapor deposition,[7] and the laser-furnace methods.[8] The laser method is known to produce high quality SWCNTs although the method is very expensive to operate. However, the laser method is less sensitive to changes in experimental conditions when compared to the chemical vapor deposition (CVD) method. In this method, small changes in the fluid flow of gaseous feedstock with time results in the formation of variety of materials with varying morphologies. This is not the case with the laser method.

If optical access to the laser generated plasma is limited to short periods (seconds), a temporal and spatial study of the plasma by optical emission spectroscopy (OES) becomes possible. In this way, the effect of experimental conditions on the plasma characteristics such as electron density, electron or plasma temperature as well the role of carbon and catalysts in the nucleation of SWCNTs can be made. In recent times only a handful of research groups have applied the OES method to the investigation of carbon nanotube synthesis. In the laser process these were applied by Arepalli *et al.*,[9,10] Ishigaki *et al.*,[11] Puretzky *et al.*,[12] and Ikegami *et al.*[13] OES was applied to the arc-discharge method by Nishio *et al.*[14] OES procedures have also been applied in less common synthesis methods which are variations of a combined plasma/CVD method such as triode plasma CVD,[15] rf thermal plasma,[16] pulsed-dc plasma-enhanced CVD (PECVD) (Ref. 17), and the microwave plasma CVD method.[18]

In most of these studies the temporal and spatial behavior of dominant emission bands such as the Swan C$_2$ bands were investigated. However, no conclusions were made as to

a)Author to whom correspondence should be addressed. Electronic mail: mkmoodley@csir.co.za.
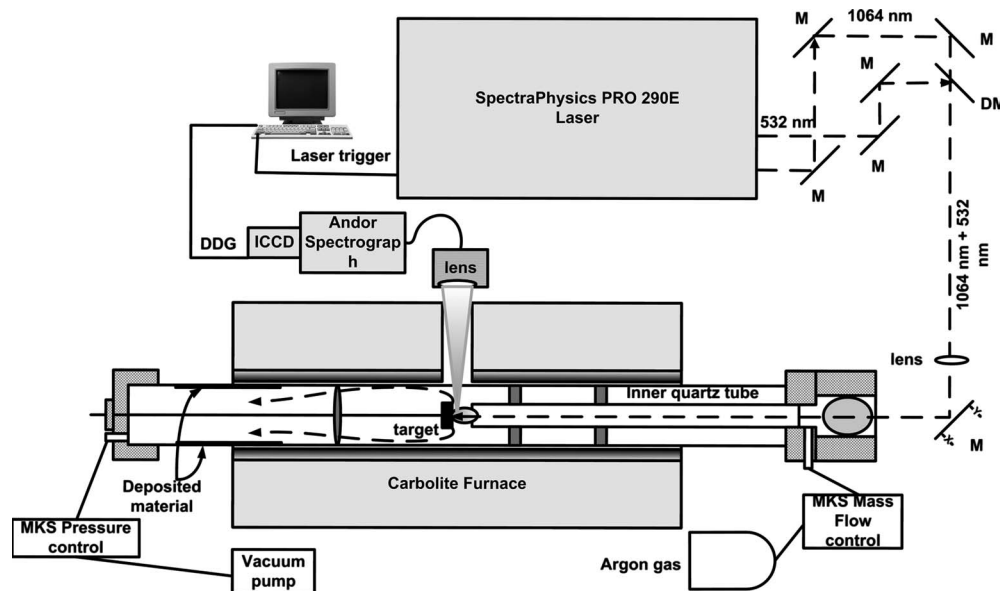b)Electronic mail: neil.coville@wits.ac.za.

FIG. 1. Experimental layout for the synthesis of SWCNTs and *in situ* plasma spectroscopy. *M*=mirror, DM=dicroic mirror.

the role of C_2 on SWCNT nucleation or if and when nucleation took place from C_2 or any other carbon species. Furthermore, in applying OES to pursue a temporal and spatial study of the electron density and electron temperature of plasma either induced by laser or by high electrical voltage discharge no group have yet deduced any link or correlation between the changes in electron density, electron or plasma temperature as evidence of nucleation of SWCNTs.

In this study, we have applied *in situ* OES to study the plasma in the laser-furnace method to synthesize SWCNTs. In particular, we have investigated the temporal and spatial behavior of C_2 as well as the electron density and electron temperature. In addition synthesized materials were characterized by Raman spectroscopy. With these results we reveal the first experimental evidence for the early nucleation and rapid growth of SWCNTs.

II. EXPERIMENTAL

A. General experimental set-up for laser synthesis of SWCNTs

The experimental set-up for *in situ* OES measurements of carbon plasmas containing transition metals is identical to the setup in which SWCNTs are synthesized. This is shown in Fig. 1. For the synthesis of SWCNTs, a Q-switched Nd: Nd:YAG (YAG) (Spectra Physics Pro290E) was operated at 30 Hz pulse repetition rate. The first and second harmonic laser pulses with energies of 350 and 720 mJ per pulse, respectively, and which were separated by a path difference equivalent to about 20 ns were made collinear by using a set of reflective laser mirror optics for each wavelength and were combined by a using a dielectric mirror. The pulse width full-width half-maximum (FWHM) was 12 and 8 ns for the 1064 and 532 nm pulses, respectively. When operated at 30 Hz, this corresponds to an average power of 10.5 W at 1064 nm and 21.5 W at 532 nm, respectively. The combined beams were focused with an antireflection coated lens of focal length F_1=1800 mm to a spot size of 3 mm onto a

cylindrical graphite composite target located at the center of an enclosed quartz tube of inner diameter 44 mm, placed in a hinged tube furnace (Carbolite). At this spot size, the energy density was 5 and 10.2 J cm^{-2} for 1064 and 532 nm, respectively. The target was pressed out of paste containing graphite, metal catalysts in the form of nickel and yttrium nitrates and Dylon® cement paste. The target was pressed in a piston and sleeve and cured at 403 K in a vacuum oven for 12 h. Thereafter, the target was fixed to a 6.4 mm diameter stainless steel rod and positioned at the center of a larger quartz tube. The target was baked at 1273 K for 4 h to allow outgassing of all unwanted chemicals so that a final target composition of 95% C, 4% Ni, and 1% Y at. % was achieved. Fixed to the front end of the quartz tube were vacuum fittings which could accommodate an optical window fixed at a Brewster's angle of 56° to minimize the reflection of the incoming laser pulses. A gas connection to allow the in-flow of argon gas was also fitted to the end of the quartz tube. The flow and pressure of the argon gas was controlled by an MKS Type 247 system consisting of a Mass-Flo® and an MKS Type 640 transducer, respectively. A second quartz tube of diameter 26 mm was positioned inside the outer quartz tube. This was done to ensure laminar flow of argon gas inside the tube. The argon gas acts as a buffer and aids in plasma confinement which improves the condition under which self-assembly of carbon atoms into SWCNTs is favored. The second function of the gas was to carry the SWCNTs to the rear of the quartz tube where they condensed on cooler regions. To produce as-prepared material containing significant amounts of SWCNTs, the laser was allowed to raster the target surface for about 30 min by means of motion controlled steering mirrors. These mirrors were positioned just before the entrance of the quartz tube. After each run, and after the system had cooled down, the material for Raman spectroscopy analysis was scrapped off the inside back-end of the quartz tube. The parameters for the synthesis of SWCNTs are summarized in Table I.

TABLE I. Operational conditions under which OES data were captured and under which SWCNTs were synthesized. As-prepared materials were labeled using the following nomenclature: samples prepared at flow rate of 150 and 200 SCCM were labeled by C and B, respectively, followed by a three digit number which is the pressure in Torr, e.g., C100 refers to SWCNTs prepared at a flow rate of 150 SCCM at a pressure of 100 Torr.

Flow rate (SCCM)	(C) 150	(B) 200
Pressure (Torr)	100	100
	400	400
	600	600

B. Experimental set-up for OES measurements

For OES measurements, the laser was operated in single-shot mode. Light emission due to ablation events were captured by an Andor CC52 optical unit which was mounted adjacent to the center of the tube furnace on an X-Y-Z mechanical translation stage. The CC52 was linked by optical fiber to the spectrograph. When the target is ablated, the plasma expands in a volume and its movement is primarily in the direction perpendicular to the target surface. In this setup (Fig. 1), the target was placed in the same axis as that of the incoming pulsed laser beams, defined as the z-axis. The collection of broad-band spectra was optimized with the aid of a diode alignment laser built-into the CC52. This allowed regions along the z-axis, through which the plasma plume propagates, to be imaged onto the entrance aperture of the optical fiber connected to an Andor ME5000 echelle spectrograph. The spectrograph, of focal length 195 mm with f/7, can simultaneously record in a spectral range of 200–950 nm for a single laser ablation event. The detector attached to the spectrograph was an Andor DH734i intensified charged coupled device (ICCD). The detector has 1024×1024 pixels with total area of 13.6 μm^2. The detector chip was Peltier cooled to $-10\ ^\circ$C for optimum performance. The overall detectable spectral range in a single acquisition was limited to 200–850 nm in a single acquisition. The entire detection system was controlled by a computer loaded with Andor Solis spectroscopic data capture software.

The hinged tube furnace was opened to an approximate angle of 40° for periods up to 6 s during which time an average of three laser ablation events was recorded. Thereafter, the furnace was allowed to regain its temperature setting of 1273 K. This process was repeated three times and the accumulated spectra were averaged to improve statistics. The ICCD had an internal digital delay generator (DDG) which was connected to the laser output trigger. Firing the laser triggered the ICCD to accept incoming signals. In the initial phase of an ablation event, there is a strong continuum signal due to Bremsstrahlung, emanating from the plasma plume. This period lasted for about 500 ns during which no recombination or emission lines of the atomic species in the plasma were detected. This is our reference point for collecting spectra. We reset this value to 0 ns. A fixed gate width of 500 ns was selected in the DDG. To track the spatial and temporal evolution of the plasma plume it was possible to increment the delay time from 0 to 1200 ns in increments of 100 ns. These measurements were then repeated but taken at different distances from the target surface along the z-axis. These were varied from 0 (target surface) to 5 mm in increments of 1 mm. The argon gas flow rate was fixed at 150 or 200 SCCM while the pressure was varied. Experimental parameters under which OES measurements was performed are shown in Table I.

C. *Ex situ* as-prepared sample characterization

To compliment the OES experimental results, the synthesis of SWCNTs proceeded as outlined in Sec. II A. The material collected after 30 min runs was characterized by Raman Spectroscopy. For Raman work about 3 mg of the as-prepared material was sonicated in 6 ml reagent grade ethanol using a Hielscher UP400S horn sonicator fitted with a tapered probe operated at 50% (200 W) power. The sample was sonicated for 3 min while kept cool in an ice bath. A few drops of this solution was placed on a standard microscope glass slide and dried on a heating mantle at 323 K for 30 min to evaporate the ethanol and produce a thin film of material on the slide. A Horiba Jobin Yvon HR800 Raman microscope was used for the Raman measurements. Fitted to the 800 mm focal length spectrograph was an Olympus BX41 microscope with a $50\times$ objective lens. Laser radiation was focused to a 150 μm spot size. The samples were subjected to two laser excitation wavelengths of 488 and 647 nm. The laser power measured at focus was about 1.5 mW for each of the laser excitation wavelengths. For uniformity, all Raman data were acquired for approximately 60 s in the range of $100-3000$ cm^{-1}.

III. MEASUREMENT OF PLASMA PARAMETERS

A. Electron density and temperature measurements

Methods used for determining plasma parameters such as electron density and electron temperature are largely based on the analysis of optically thin emission spectral lines, i.e., lines that do not suffer self-absorption, do not show distorted line widths or are not saturated; otherwise this will lead to incorrect measurements of plasma parameters. The most frequently used method to measure electron density in laser induced plasmas is by measuring the Stark broadened line profile of a particular emission line of the collected emission spectrum. The Stark effect is due to the collisions of the emitting atoms with electrons and ions which result in the broadening of the line and a shift in the peak wavelength.[19–21] In this study we calculated the electron density by measuring the Stark broadened profile of the CII ion emission at 283.7 nm $(2s2p^2-2s^23p)$. Doppler broadening was neglected.[22] In this work, the uncertainty in the electron temperature measurements is due to the uncertainty in the values of the oscillators strengths as found in the National Institute of Standard and Technology (NIST) database.[23] The contribution to line width may be expected to contribute significantly in slightly ionized gas systems where ions interact with neutral atoms.[19] However, in the case of laser generated ablation plasmas, the plasma is highly ionized in the early stages or during the propagation times investigated so that the density of neutral perturbers is very low. Furthermore, the oscillator strength of the CII at 283.7

TABLE II. Emission line parameters of CII lines taken from NIST. (Ref. 23) These were used to calculate the electron plasma temperature.

Wavelength (nm)	$A_j g_j (\times 10^8)$ s^{-1}	Upper energy level E_j (eV)
250.9	1.81	18.67
251.3	3.25	18.65
283.7	1.59	16.33
657.9	1.45	16.33
723.3	1.41	16.33
723.8	2.53	16.33

nm is 0.096.[23] This value is relatively very weak in comparison to other emission lines. Therefore, broadening attributed to resonance pressure was neglected.[24] The quadratic Stark effect which relates to the FWHM of the broadened emission line and that of electron density without ionic contribution is given by the relation[19]

$$\Delta\lambda_{FWHM} \approx 2 \times 10^{-16} w N_e, \qquad (1)$$

where w is the electron impact parameter, which can be incorporated for different temperatures.[19] The values for the electron impact parameter w can be found in Refs. 19 and 24. For the CII ion emitting at 283.7 nm, $w = 0.0928$ Å at 10 000 K. We assume in these calculations that the plasma is in local thermodynamic equilibrium (LTE) which is a state in which the temperature of the Boltzmann and Saha equations is equal to that of the Maxwell–Boltzmann velocity distribution of free electrons.[25] This assumption has been validated in many studies on laser induced plasmas under various experimental conditions similar to that undertaken in this study.[26] In this study we employed the Boltzmann plot method to determine to kinetic electron temperature.[19] We use the following relation:

$$\ln\left(\frac{I_{ji}}{A_{ji} g_j}\right) = -\frac{1}{kT_e} E_j^Z + \ln\left(\frac{hc N^Z}{4\pi U^Z(T)}\right), \qquad (2)$$

where I_{ji} is the intensity of the emitted line of wavelength λ_j, h is Plank's constant, c is the speed of light, A_{ji} is the atomic transition probability, g_j is the degeneracy of level j, Z is the ionization and equal one for singly charged ions, and $U^Z(T)$ is the partition function. Equation (2) takes the form of a linear equation which can be plotted. By plotting the ordinate $\ln(I_{ji}/A_{ji}g_j)$ versus the abscissa E_j^Z with its coefficient, $1/kT_e$ being the gradient of the line from which we can deduce the kinetic electronic temperature. The accuracy of the method is improved if more than several emission lines are plotted and if there is a larger range of E_j^Z values.

In this work, the electron temperature was evaluated using six emission lines of CII. These lines are given in Table II. The parameters were taken from the NIST spectroscopic atomic database.[23]

IV. RESULTS

A. Characterization of as-prepared materials by Raman Spectroscopy

Figures 2–5 show Raman spectroscopic data of as-prepared laser synthesized material. These samples were ob-tained under conditions outlined in Table I during which the laser was operated at a pulse repetition rate of 30 Hz. Two laser excitations were utilized to resonantly excite semiconducting type nanotubes with 488 nm and metallic nanotubes with 647 nm.[1] Radial breathing modes (RBM) are shown in Figs. 2(a)–2(f) and 3(a)–3(f). The D and G bands of the spectra are shown separately in Figs. 4(a)–4(f) and 5(a)–5(f).

As is typical in the synthesis of SWCNTs, a distribution of the SWCNT diameters including the semiconducting and metallic types were found in all the as-prepared samples. To quantify this distribution, the RBM bands were fitted with Lorentzian curves with the peak of each curve represented by its wavenumber position and intensity. In this paper, we did not associate the chiral indices value (n, m) of SWCNTs with any of these peaks. We only track the relative changes of each major peak with respect to the changes in the argon gas pressure and flow rate. Since it is easier to understand tube diameters in terms of nanometers than wavenumbers,[27] we applied Eq. (3)

$$\varpi_{RBM} = \frac{c_1}{d} + c_2, \qquad (3)$$

where ϖ_{RBM} is radial breathing mode frequency, d is the tubes diameter in nanometer, c_1 and c_2 are constants. Experimental and theoretical values of these constants in published data vary between 215 and 260 cm^{-1} for c_1 and between 0 and 20 cm^{-1} for c_2.[27] We choose $c_1 = 215$ and $c_2 = 18$ cm^{-1}, taken from Maultzsch *et al.*[28] Using the above relation and applying it to the Raman spectra, we observe that the nanotube diameters vary in the range 1.1–1.6 nm for semiconducting types (Fig. 2) and between 1.1 and 1.8 nm for metallic type tubes (Fig. 3). At a low pressure of 100 Torr, the Raman signals are relatively weak which is indicative of a low concentration of SWCNTs while the highest intensities of RBM signals were obtained at 400 Torr for both flow rates of 150 (C) and 200 sccm (B).

At both flow rates (C and B), the intensities of the Lorentzian's fitted to the raw spectra vary with pressure for the semiconducting type nanotubes. It was found that lower pressures favor larger tube diameters while higher pressures favor smaller tube diameters. The peak at 200 cm^{-1} appears to be associated with the dominant tube. In the case of metallic tubes excited by a 647 nm laser, the tube at around 190 cm^{-1} dominates and is completely favored at higher pressures. Hence the pressure and flow rate influences the nature of the nanotubes that are formed.

Figures 4 and 5 show D and G bands. The G band has been deconvoluted to show the G$^-$ and G$^+$ peaks. The D band or mode is disorder induced. It is observed because its intensity is enhanced in a double-resonant process and its Raman frequency shifts with laser excitation energy. The intensity of this peak increases with disorder. The contributions to the disorder are from tubular defects such as vacancies, sharp bends in the tube, hemispherical closed ends, or from chemical or functional groups attached to the tube. The second order overtone of the D mode is noted as D* (not shown in the Raman spectral data) is also a double resonant process and is located between 2600 and 2700 cm^{-1}. It is very strong
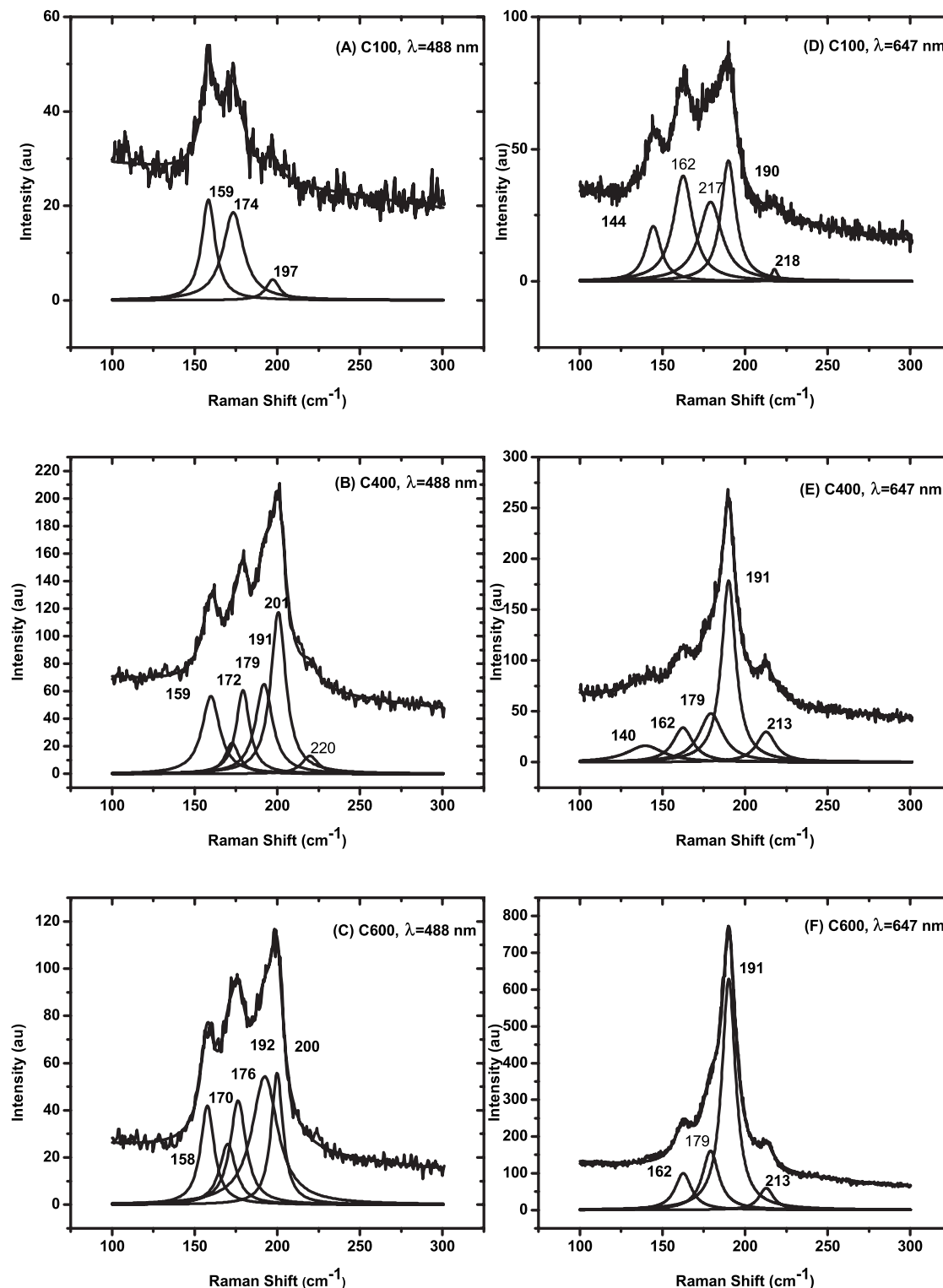
FIG. 2. Raman spectroscopy of laser-furnace as-prepared samples showing the RBM bands, C series. Plots of Figs. 2(a)–2(c) excited by a 488 nm excitation line bring semiconducting type SWCNTs into resonance and Figs. 2(d)–2(f) excited by 647 nm exciation line which metallic SWCNTs preferrably resonant.

and always present in SWCNTs and often stronger than the D band. In this study, to obtain a measure of defect concentrations, we have normalized the D mode intensity to that of the D^* mode intensity.[29] A low D/D^* value is associated with material with low defect concentration. The results for this analysis are shown in Table III.

We found that the lowest and hence the best D/D^* values were achieved at the higher pressures and flow rates.

Thus, low argon gas pressures gives rise to a high defect content implying that a low pressure is not conducive for promoting the self-assembly of carbon atoms into SWCNTs. At low pressures, the ablated materials travel at high velocity outward, thus reducing the probability of self-assembly. Samples collected under different pressure conditions also have different texture. For example, the sample corresponding to B400 was more "spongy" while C100 appeared to be
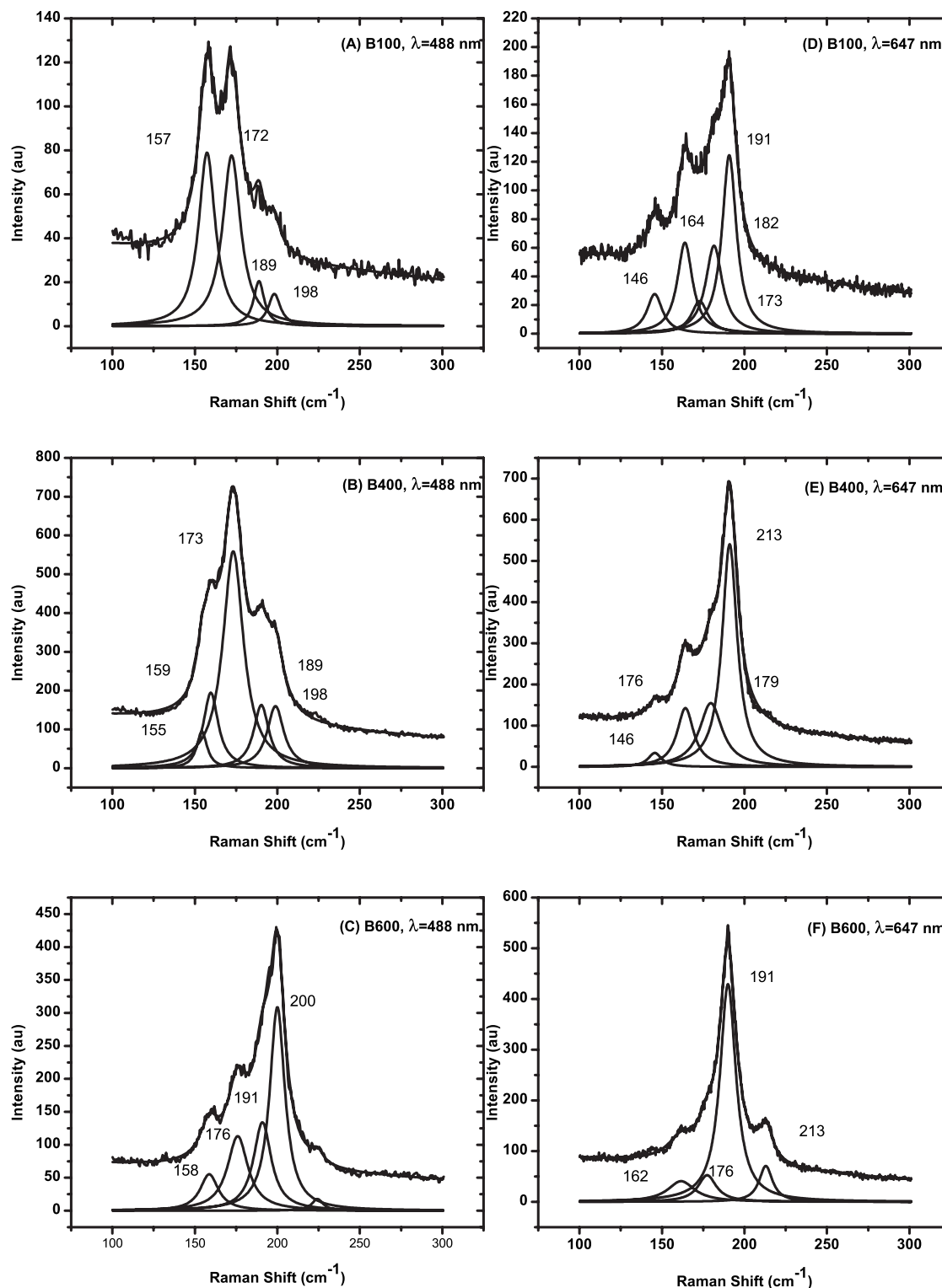
FIG. 3. Raman spectroscopy of laser-furnace as-prepared samples showing the RBM bands, B series. Plots of Figs. 3(a)–3(c) excited by a 488 nm excitation line bring semiconducting type SWCNTs into resonance and Figs. 3(d)–3(f) excited by 647 nm excitation line which metallic SWCNTs preferrably resonant.

more granular like. This material can be thought of as consisting of long strands of "spaghetti," i.e., long SWCNTs with reduced defect concentration while a granular texture implies shortened SWCNTs. Shorter nanotubes will contribute significantly to the D band intensity because as the tubes get shorter, the contribution by the ends become significant relative to the Raman signal attributed to the stretching mode or G band.

B. Changes in the temporal and spatial intensities of dominant C_2 Swan band emissions

Optical emission spectra emanating from the laser generated plasma were recorded. The pressure and flow rate of argon gas when used to record the spectra are shown in Table I. All elemental species (neutrals and ions), were identified at a furnace temperature of 1273 K. While the spectra was
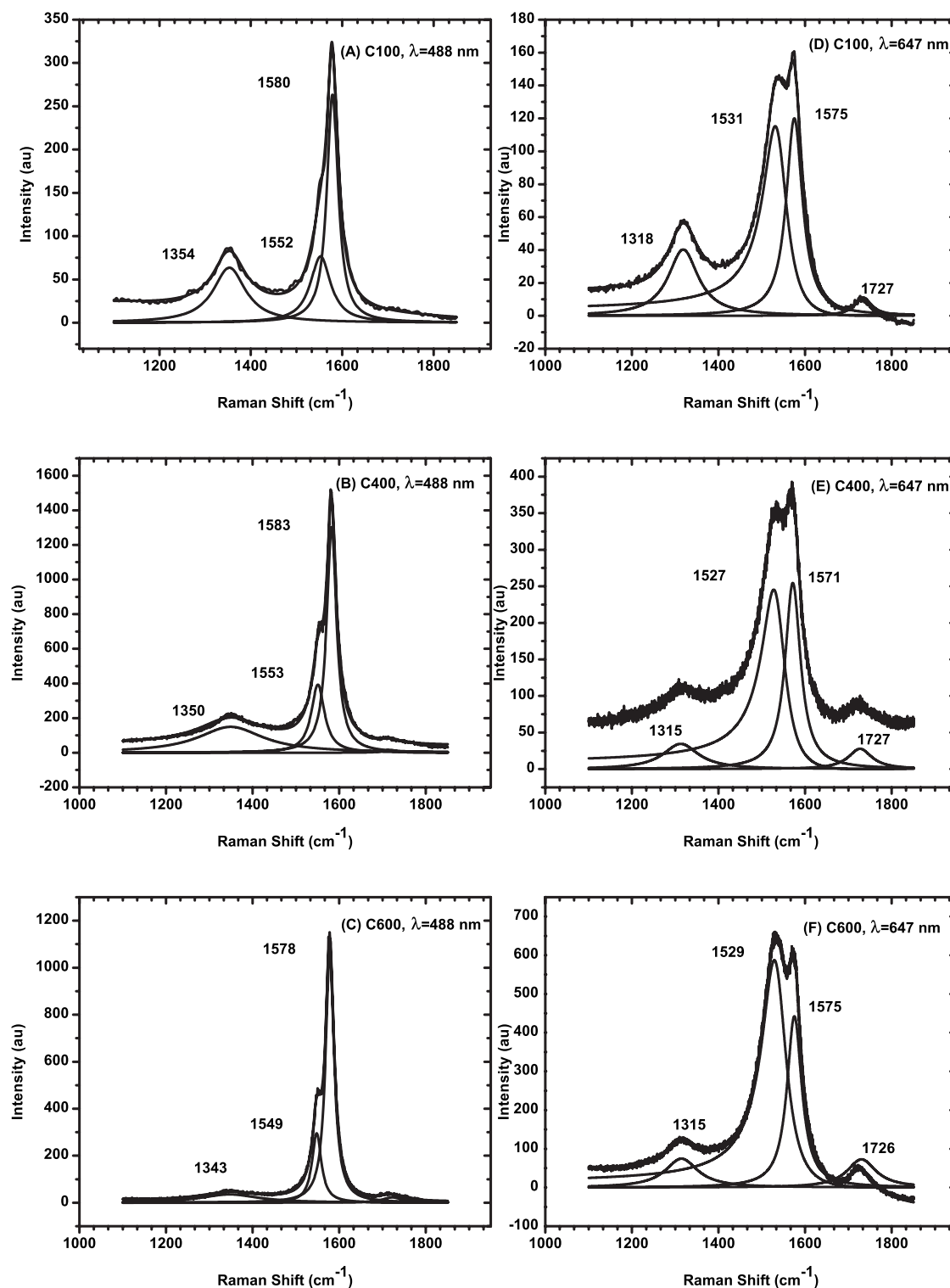
FIG. 4. Raman spectroscopy of laser-furnace as-prepared, C series samples showing the D, G⁻, and G⁺ bands. The spectra were fitted by Lorentzians, while the G⁻ peak of metallic tubes which were resonantly excited by the 647 nm laser line was fitted Breit–Wigner–Fano (BWF) formula.

dominated by yttrium atomic emission lines, no plasma analysis was possible using these lines due to the lack of atomic spectral data in available current database's. Instead, the emission lines of carbon were chosen. In this regard we were able to detect only two emission bands of C_2, i.e., those of the Deslandres D′ Azambuja (DDA) ($C\,^1\Pi_g - A\,^1\Pi_u$) and Swan ($d\,^3\Pi_g - a\,^3\Pi_u$) band systems.[30]

The DDA was relatively weak and were very close to and dominated by emission lines from the other elements

such as Ni, Y, and Ar. This made analysis difficult and no analysis of these bands was made. The Swan bands on the other hand were more distinct and were used to study the temporal and spatial behavior of the plume emissions. Furthermore, these molecules are proposed to be one of the main precursors leading to the formation of SWCNTs.[31,32] Figs. 6(a)–6(d) shows emission spectra characteristic of C_2 Swan bands. Peaks associated with the (0, 0), (1, 1), and (2, 2) vibrational bands are prominent at 516.5, 512.9, and 509.9
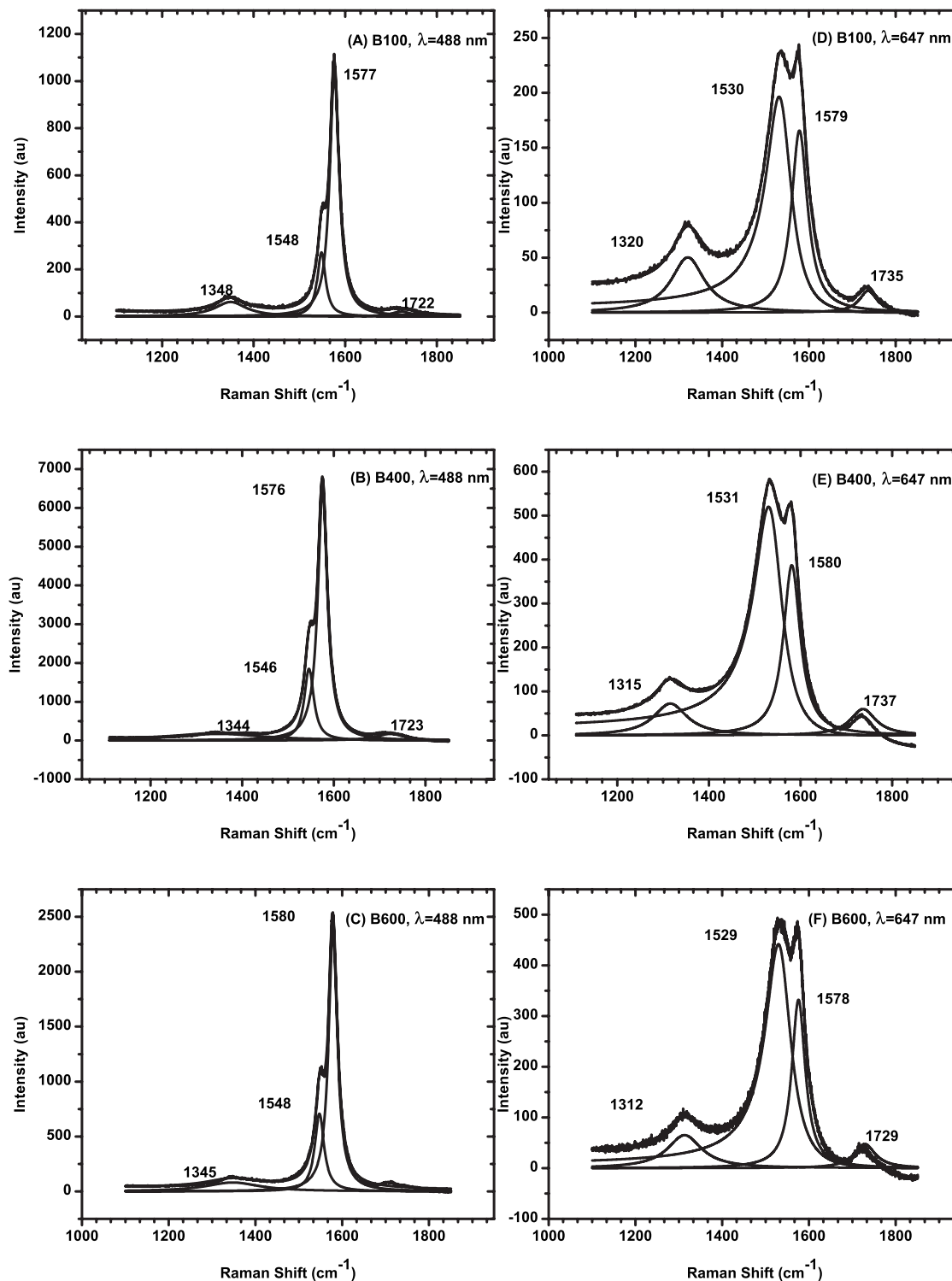
FIG. 5. Raman spectroscopy of laser-furnace as-prepared, B series samples showing the D, G^- and G^+ bands. The spectra were fitted by Lorentzians, while the G^- peak of metallic tubes which were resonantly excited by the 647 nm laser line was fitted BWF formula.

nm, respectively. These were recorded at pressures between 100 and 600 Torr at an argon gas flow rate of 200 SCCM with delay time in increments of 100 ns 1mm away from the target surface. This delay time refers to the time after which recombination between electrons and ions resume, leading to the emission of characteristic lines corresponding to various electronic transitions in the ions and/or atoms that constitute the plasma. Prior to the start of recombination, the emission is broadband and is referred to as the continuum emission. In

our experiments this continuum emission lasted for about 500 ns after which distinct emissions lines started to appear. As a consequence, all references to delay times refer to the time after the disappearance of the continuum.

The emission spectra of Figs. 6(a)–6(d) show a fluctuation in the Swan band intensities with pressure. Figures 7(a)–7(d) show plots of the temporal and spatial change in the emission intensity when the Swan band intensity is plotted as a function of distance from the target surface at dif-

TABLE III. The ratio D/D* is an indication of defect concentration in SWCNTs. These values were obtained from Raman spectra of as-prepared SWCNT samples excited at 488 nm for semiconducting nanotubes and 647 nm for metallic natured nanotubes.

Sample	D/D* (488 nm)	D/D* (647 nm)
C100	1.71	1.18
C400	0.49	0.53
C600	0.35	0.61
B100	0.80	1.04
B400	0.23	0.67
B600	0.46	0.68

ferent pressures and two different argon gas flow rates. There is a noticeable difference in the behavior of the Swan band intensities with distance from the target surface for 150 SCCM [Fig. 7(a)] and 200 SCCM [Fig. 7(b)] flow rates. For a flow rate of 150 SCCM, the Swan band intensities measured at 100, 400, and 600 Torr weaken consistently, almost converging to a common point.

However, at a flow rate of 200 SCCM, the Swan band intensity oscillates with decreasing amplitude up to a distance of 3 mm and thereafter decays quickly. Between 1 and 2 mm, there is a sudden drop in the emission intensity which recovers between 2 and 3 mm. This phenomenon was observed at all delay times between 100 and 1200 ns after the onset of recombination while the gate width of the ICCD was fixed at 500 ns.

C. Electron density and temperature measurements

The electron density was determined by the Stark broadening [Eq. (1)] of certain spectral lines of CII at 283.7 nm. The spatial changes in the laser induced plasma at a furnace temperature of 1273 K was measured at the target surface and tracked to a distance of 5 mm away from the target surface while keeping the delay settings on the ICCD fixed at 100 ns. Figures 8(a) and 8(b) show the electronic density profile at an argon flow rate of 200 SCCM and at pressures of 400 and 600 Torr. Initially, at the instant of ablation, the electron density in the evolving plasma is the same for all pressures and flow conditions. However, as the plasma expands with time the pressure and flow begin to influence the rate of expansion, decay, and eventual extinction of the plume. Higher gas pressures increase the plasma confinement, i.e., the plasma expands less than at lower pressures. Therefore, as the plasma expands, the electron density in the
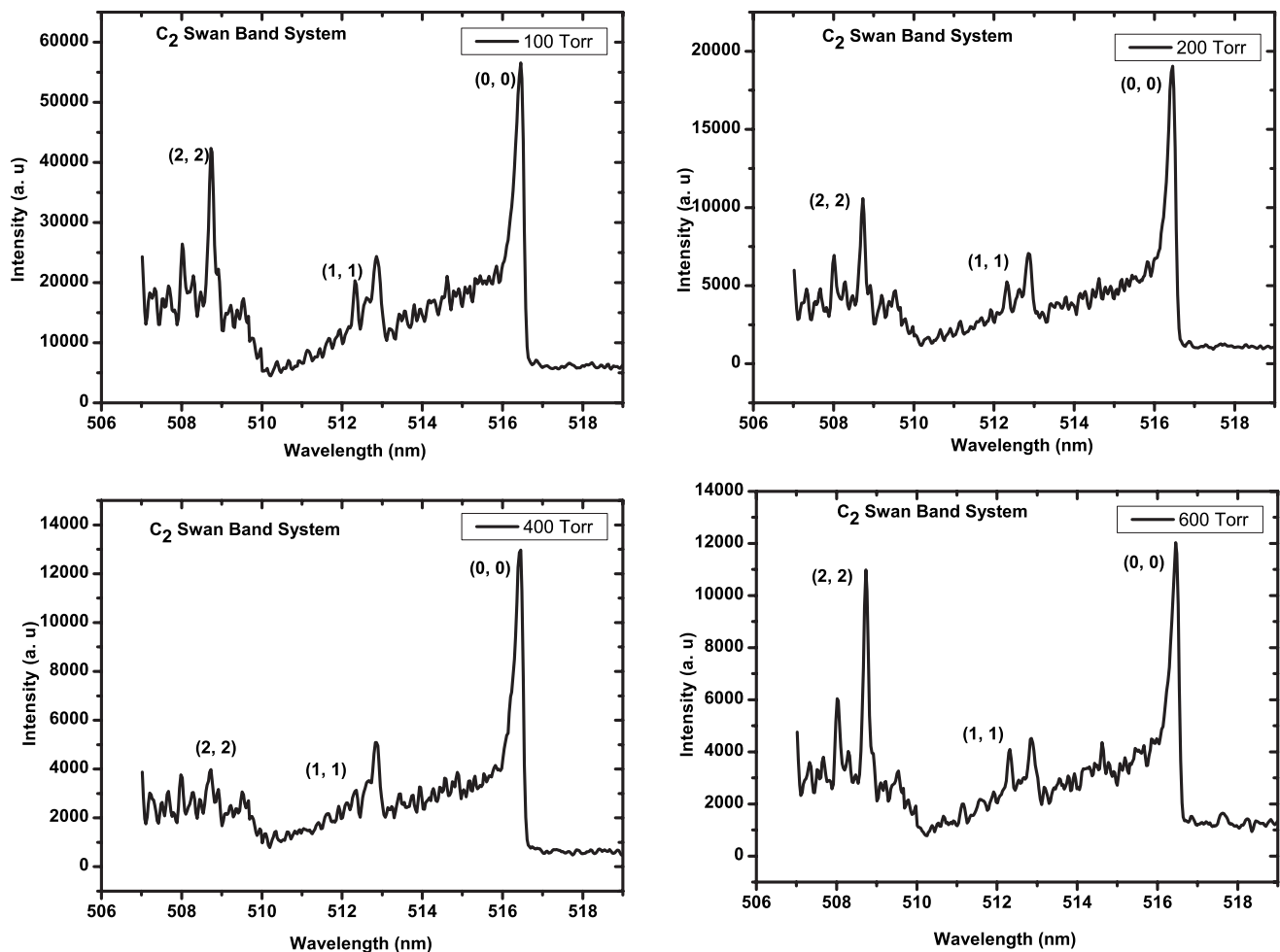

FIG. 6. (a)–(d) show the emission spectra characteristic of the Swan band system of C_2 recorded at 1 mm from the target surface, 200 SCCM Ar flow, T = 1000 °C, and different pressures. The emission peaks of 516.5, 512.9. and 509.9 nm are associated with the (0,0), (1,1), and (2,2) vibrational bands of C_2. (a) 100, (b) 200, (c) 400, (d) 600 Torr.
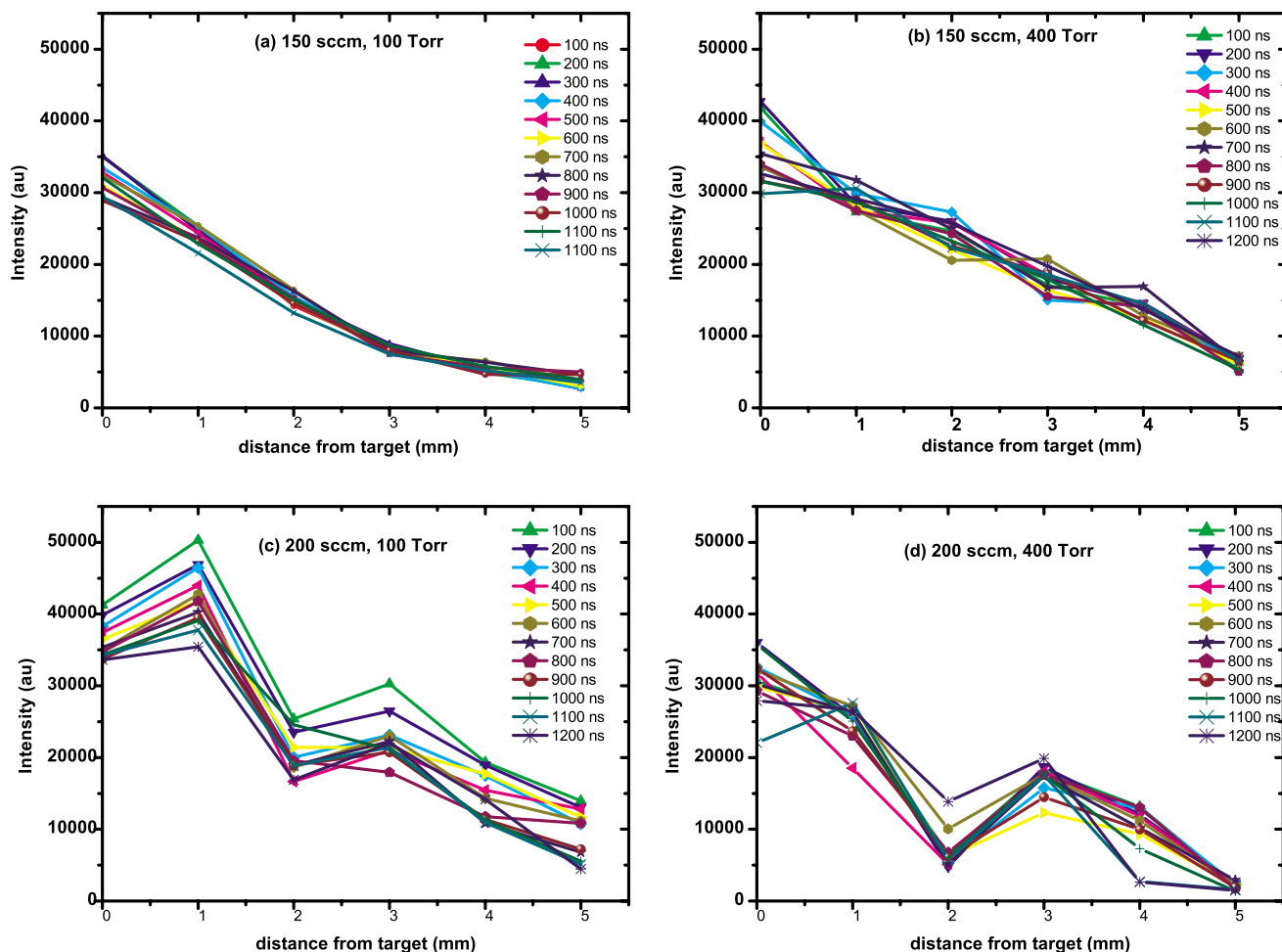
FIG. 7. (Color online) The spatial and temporal profile of the C_2 Swan band intensities (a) 150 SCCM, 100 Torr; (b) 150 SCCM, 400 Torr; (c) 200 SCCM, 100 Torr; (d) 200 SCCM, 400 Torr.

plasma is expected to decrease faster than at a higher pressure. Hence the gradient of plot in the Fig. 8(a) (0.23) is higher than that of the plot in Fig. 8(b) (0.16). The drop in electron density is indicative of a recombination process between ions and electrons in the plasma, it would therefore mean that at 400 Torr and 200 SCCM, the recombination process was more favorable than the process that takes place at pressure of 600 Torr and 200 SCCM. Figure 9 shows the temporal evolution of the electron density measured at 1 mm from the target surface at a pressure of 400 Torr and argon flow rate of 200 SCCM. Again, we observe approximate 1/time decay. However, there is a noticeable appearance of a small rise in the electron density between 0.7 and 1.0 μs. This behavior was not observed at other pressures and flow conditions.

Figures 10(a)–10(d) show the change in electron temperature with distance from the target surface for argon pressures of 400 and 600 Torr and at flow rates of 150 and 200 SCCM. We observe that the electron temperature is higher at the target surface at a pressure of 600 Torr due to increased plasma confinement. At a higher flow rate, there is an increase in the rate of collisions between argon gas atoms and plasma ions, which will reduce the kinetic energy of the expanding plasma plume. Furthermore, a faster recombination between electrons and ions will be promoted.

The temporal changes in the electron temperature measured at 1 mm from the target surface has been plotted for two pressure conditions, namely 100 (B100) and 400 Torr (B400) under an argon gas flow of 200 SCCM. These plots are shown in Figs. 11(a) and 11(b). With time, there is a drop in the electron temperature. However, the drop is sharper at a pressure of 400 Torr than at 200 Torr. Furthermore, at 400 Torr, there is a distinct increase in electron temperature between 0.7 and 1.0 μs. A change of electron temperature is estimated from the graph to be approximately 2596 K. This observation was less pronounced at a pressure of 200 Torr where a smaller change of 761 K was recorded.

V. DISCUSSION

It is has been suggested in the carbon nanotube research community that C_2 dimers could possibly be the precursors to nanotube growth.[30,31] Previous reports of *in situ* OES observations in carbon nanotubes synthesis[9,12–14,18,33–35] refer mainly to the detection of C_2 species and the intensity changes observed when external parameters are changed and optical imagery of the plume dynamics. No conclusions on the possible nucleation of nanotubes and the role that C_2 has are made. However, a recent study by Marchand *et al.*[36] observed the CVD growth of carbon nanotubes by *in situ* field
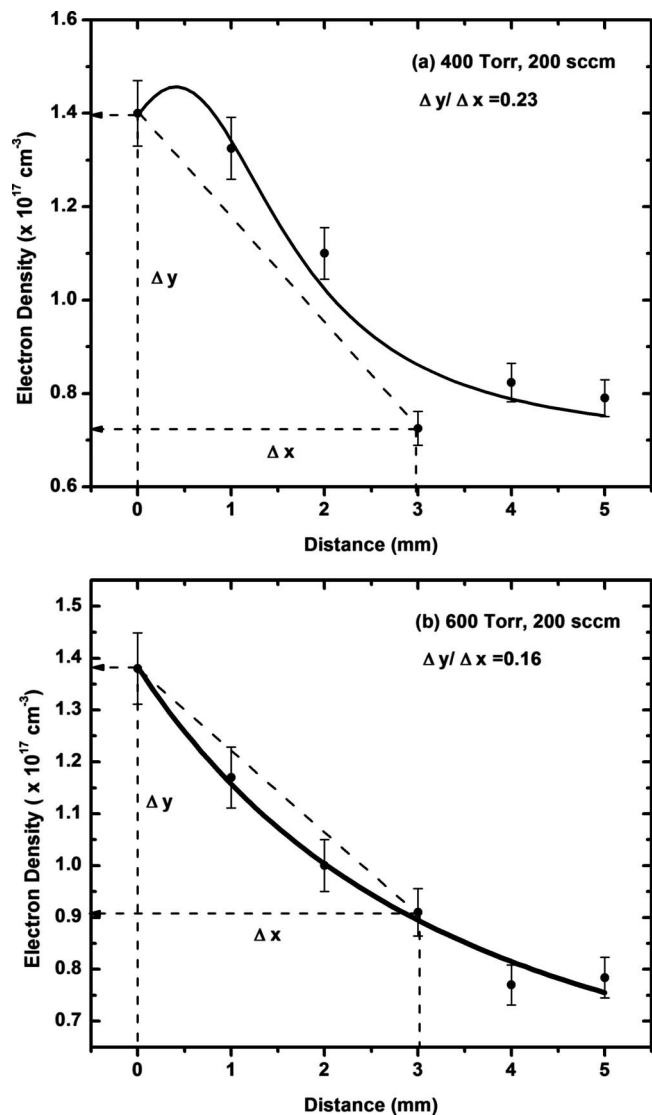
FIG. 8. The spatial profile of the electron density measured at 100 ns after recombination for (a) B400 and (b) B600.
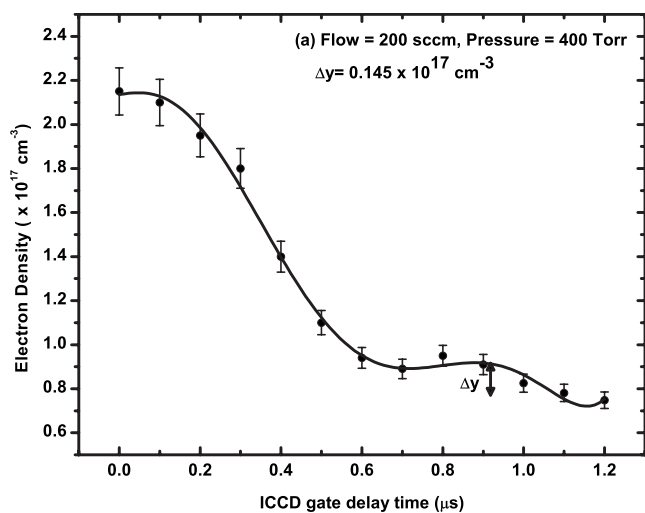

FIG. 9. Temporal profile of the electron density measured at 1 mm from the target surface, 100 ns after recombination at argon pressure of 400 Torr, and flow rate of 200 SCCM.

emission spectroscopy. From this study, the authors concluded that the growth proceeds by a "corkscrew" motion, out of the plane of the catalyst surface via C_2 addition at the interface of the catalyst and the growing nanotube. Another recent computational study by Ohta *et al.*,[37] modeled the growth of SWCNTs on a Fe cluster. In this study, a continuous supply of carbon atoms at the Fe–C interface was assumed which resulted in rapid growth rates of 0.043 Å/ps which is equivalent to a growth rate of 4.3 m s^{-1}. Therefore, under favorable conditions, when the carbon feedstock is rapidly available, Ohta *et al.*[37] suggested that the rapid nucleation at the metal–C interface and growth of nanotubes can be achieved.

In all work described in this paper, we were able to make SWCNTs where the quantity and quality depended on the experimental conditions. An argon pressure setting of 400 Torr and flow rate of 200 SCCM produced the most and highest quality of SWCNTs as determined by the relatively strong Raman RBM bands [Figs. 3(b) and 3(e)] and G bands

[Figs. 5(b) and 5(e)]. The defect concentration for this sample was indicated by a low ratio value of D/D* (Table III).

The changes in C_2 Swan band intensity as a function of time and distance from the target surface, Figs. 7(a)–7(d), is indicative of the history of C_2 in the plasma plume. We observe that the initial intensity and concentration of C_2 in the various experiments is independent of pressure and flow rate since the laser energy was kept constant. At low pressures and a flow rate of 150 SCCM [Fig. 7(a)], the C_2 intensity decreases monotonically with distance from the target surface and shows little variation with different delay times as the plasma plume expands adiabatically, i.e., the molecule experiences very little collisions or cluster formation. An increase in pressure to 400 Torr showed that the rate of expansion was reduced and a variation in the intensity with delay time and distance was observed. Fluctuations in the intensity are attributed to energy released due to cluster formation (ordered or amorphous) or collisions between C_2 and/or other plasma constituents.

In Fig. 7(c), the fluctuation in intensity is more pronounced when the flow rate is increased to 200 SCCM when the pressure is held at 100 Torr. The drop in intensity is clearly not monotonic. There is a sharp rise in intensity between 0 and 1 mm, then a sudden drop at 2 mm. The initial rise could be attributed to energy released when C_2 recombines with free C atoms to form sp^3/sp^2 clusters similar to diamondlike-carbon (DLC) material.[38] However, we can discount the formation of DLC, since the characteristic broad D-G band typical of DLC structures was absent in all Raman spectra. C_3 molecular species whose emission bands are well known were not observed in any of the emission spectra investigated. Figure 7(d), shows the largest drop in C_2 emission intensity. This occurs within 2 mm from the target surface and is followed by a rise in intensity at 3 mm. Correlating these observations between the plots and the values of D/D* in Table III, the following interpretations of physical processes occurring in the plasma plume could be described. Under unfavorable SWCNT synthesis conditions, the C_2 in-
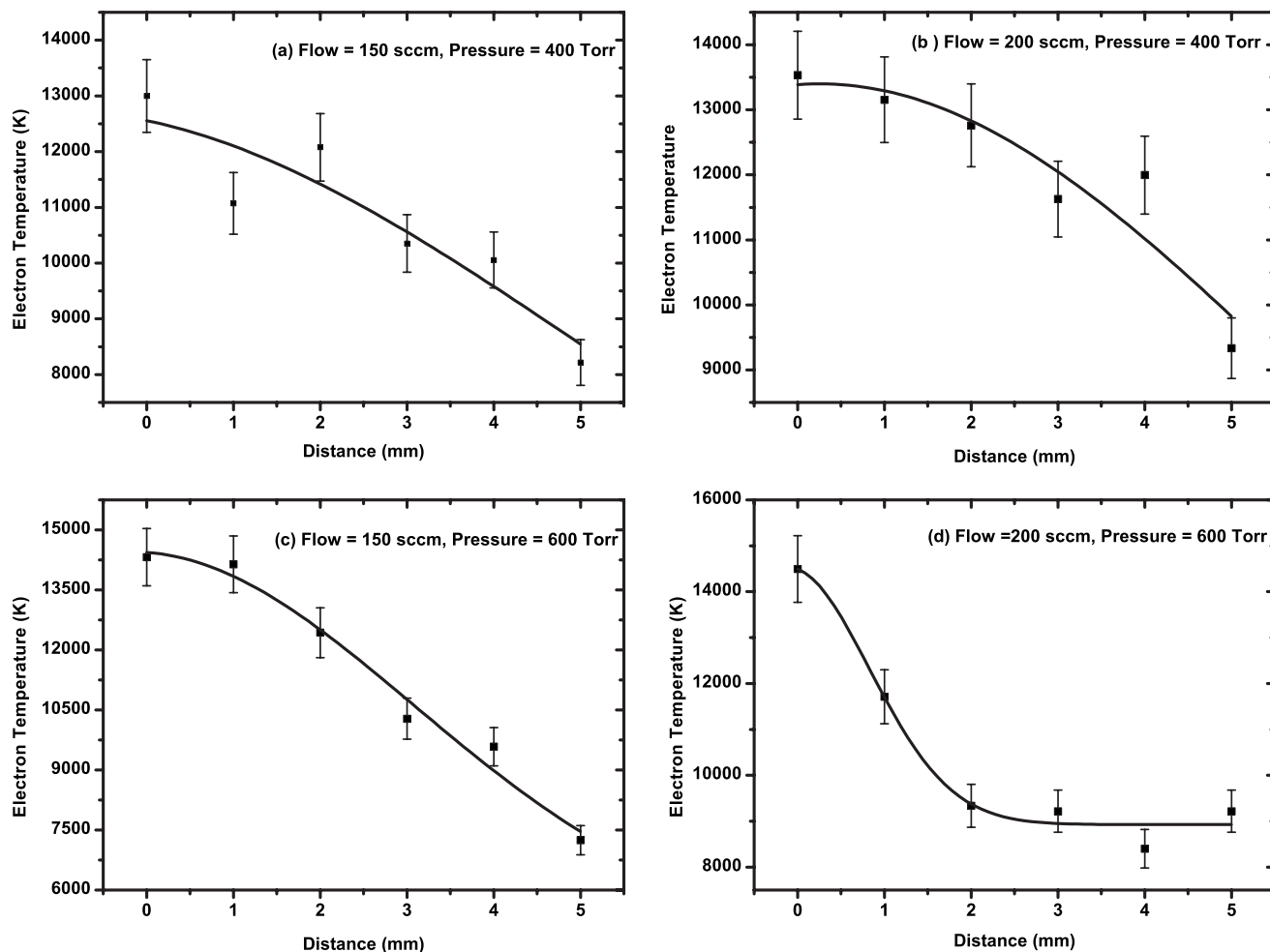
FIG. 10. The spatial profile of the electron temperature measured at 100 ns after recombination (a) 150 SCCM, 400 Torr; (b) 200 SCCM, 400 Torr; (c) 150 SCCM, 600 Torr; and (d) 200 SCCM, 600 Torr.

tensity drops with time and distance due to adiabatic expansion. When the conditions become favorable, fluctuations in the C_2 intensities occur and when the conditions are optimal, there is a sharp drop in intensity of C_2 species followed by an apparent rise in their concentration. This phenomenon relates to the abundance of C_2 is under favorable conditions, it becomes a building block for another ordered superstructure in exothermic reaction. This energy is released into the remaining plasma constituents. Hence, molecules such as C_2, would be thermally re-excited resulting in higher spectral emission levels.

Electron density measurements were measured at 400 Torr and 200 SCCM as a function of distance. The data revealed decrease 3 mm from the target, indicating that when conditions are favorable, ions and electrons recombine faster to form atoms and molecules than when conditions are not favorable [Figs. 8(a) and 8(b)]. This corresponds to the sharp drop in C_2 intensity in this region. Furthermore, the electron temperature measurements show that under the best synthesis conditions, an electron plasma temperatures exceeding 10 000 K is maintained for longer distances from the target surface [Figs. 10(b)]. This is consistent with the work of Ohta *et al.*[37] where it was shown in MD simulations, that an electron temperature of T_e=10 000 K was conducive to the

growth of SWCNTs nucleated on a cluster of Fe atoms. Rapid growth was favored when either C or C_2, was directly available at the metal-carbon boundary.

In their studies of the temporal and spatial evolution of C_2 in 100 mTorr helium by laser ablation, Harilal *et al.*[39,40] have shown that when the laser fluence on the target was 12 J cm^{-2}, a single C_2 peak at approximately 1.4 μs after ablation was observed. When the fluence was increased to 29 J cm^{-2}, a faster second C_2 emission peak appeared at an earlier time of about 700 ns. Both peaks were attributed to different recombination processes leading to the formation of C_2. At lower fluences the reaction is due to collisions between electrons, C_n(n>2) and neutrals whereas for high laser fluences it is due to electron-ion and ion-ion recombination reactions.[41]

In our case, the laser fluences were less than 12 J cm^{-2} with the experiments performed in flowing argon gas instead of a pressurized helium environment of 100 mTorr. It was observed from Fig. 7 that C_2 is immediately detected and that even with delay times ranging from 100–1100 ns, the variation in C_2 intensities at a particular point drops off with distance due to adiabatic expansion. However, as the conditions become favorable for SWCNT synthesis, fluctuations observed in C_2 can be attributed primarily to nucleation of
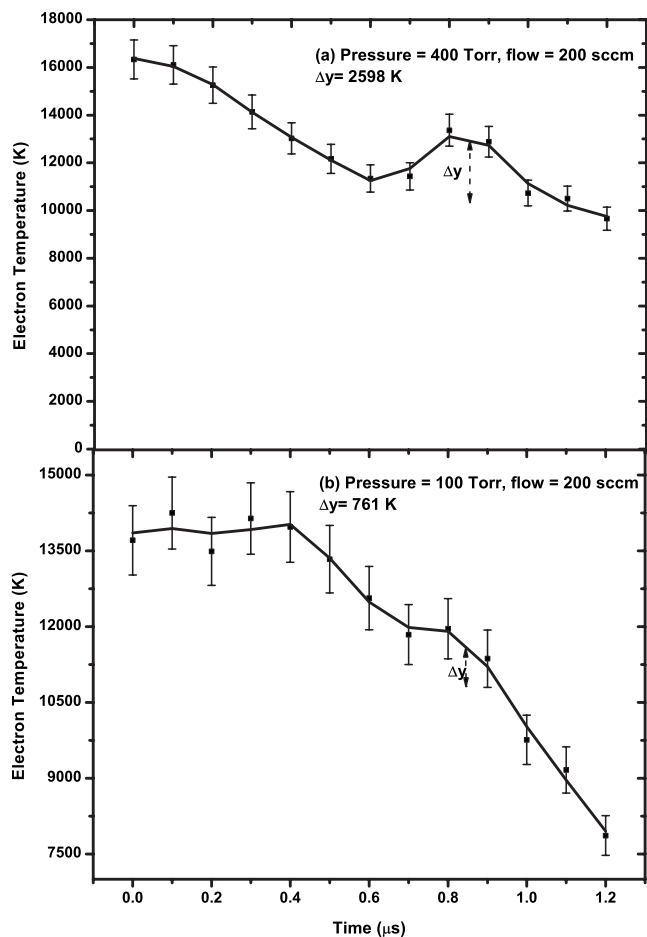
FIG. 11. The temporal profile of the electron temperature measured at a distance of 1 mm from the target surface (a) 200 SCCM, 400 Torr and (b) 200 SCCM, 100 Torr

nanotubes and rapid carbon uptake on the carbon-metal nanoparticles. A recombination process forming C_2 from CII also occurs which adds to the growth of SWCNTs.

In Fig. 9, a temporal plot of the electron density measurements made at an argon pressure of 400 Torr and flow rate of 200 SCCM are shown. Again, between 0.7–1.1 μs a small but broad peak at about 0.9 μs was observed only under optimum conditions possibly due to the heat generated by recombination of CII and by nucleation. The heat generated as a result of recombination, nucleation and rapid growth of SWCNTs is seen more clearly in the temporal evolution of the electron temperature shown in Figs. 11(a) and 11(b) where the temporal behavior was measured at 1 mm from the target surface. For this measurement, the emission lines of CII were used to determine the electron temperature.

The contribution of recombination of CII into C_2 as a major contributor to the heat of formation can be discounted for two reasons: (i) there is already a relatively high concentration of C_2 at 1 mm as shown in Figs. 7(a)–7(d) and (ii) the expansion velocity,[42] $v \propto (1/m)^{1/2}$, (where m is mass of the species) which means that CII would have a much higher expansion velocity than C_2 and would therefore have a better chance of recombining further away from the target when the plume has cooled due to adiabatic expansion. Therefore, the

rise in the electron temperature at between 0.6–1.0 μs [Fig. 11(a)], can be attributed primarily to the nucleation and the rapid growth of SWCNTs. Under optimal synthesis conditions it is expected that more heat due to the exothermic reaction would be generated than under unfavorable conditions. This is exactly what has been observed in plots Figs. 11(a) and 11(b). A larger Δy value which corresponds to a rise in plasma temperature was measured at a pressure of 400 Torr and 200 SCCM flow of argon which was the optimal condition for SWCNT synthesis.

A. Growth Model

In the laser synthesis of SWCNTs, growth takes place on metal catalysts that are ejected from the target surface.[43] Prior to ablation, and due to the manner in which the target is made, the metal catalyst particles (solute) are already covered by polycrystalline graphite (solvent). Ramping up the furnace to high operating temperatures promotes the formation of metastable carbides at the graphite–metal interface.[44] X-ray diffraction (XRD) pattern of the target prior to ablation confirms the presence of Ni_3C.[22,45] The laser energy deposited at a point at the target surface within 15 ns FWHM (Sec. II A), causes the heating rate at this point to rise to an estimated $\approx 10^{12}$ K s^{-1}. The surface temperature of the target rises to a peak value of approximately 45 000 K.[22] The energy transfer in the target takes place via electronic and vibrational excitation and results in the explosive ejection of target material. The amount of material ejected in a single laser shot was calculated to be between 10^{18}–10^{19} atoms. This material consists of nanoparticulates, molecules, ions, and electrons that form the basis of the plasma plume.

The ejected graphite-carbide-metal (GCM) nanoparticles are between 5 and 15 nm in diameter.[46] Due to the high curvature, the interfacial carbide layer is strained as a result of lattice mismatch in the GCM. At high temperatures, the carbide segregates,[47] and decomposes into C and Ni[48] causing an increase in electronic activity of Ni. The carbon from the decomposed carbide prefers to increase its coordination.[49] This results in the volume, which the segregated carbon at this region occupies to increase causing it to push into the graphite layers above. A fullerene cap may be initiated when stresses in the hexagonal graphite network are relieved by the Stone–Wales rearrangement which results in the transformation of a hexagon into a pentagon, lowering the energy and improving the stability of the lattice. The pentagon formation in a hexagonal dominated lattice results in a lifting of the C structure out of the plane of the catalyst. The formation of pentagons has been shown to be energetically favorable. In simulations performed by some groups on the nucleation of fullerenes[50–52] this process becomes the driving force for the nucleation of a nanotube. The diameter of the resulting tube will depend on the catalysts size, curvature, rims, or edges and other surface contours which result in the minimization of the C–Fe bond energy. In the case of larger spherical catalyst particles, many nucleation sites will be possible leading to multiple tube growth as observed in transmission electron microscopy observations.[53,54]

For continued growth, an external carbon source is required. In the case of laser ablation, carbon in the form of C and C_2 is readily available in the plasma plume. Assuming the catalyst particles then a single tube will be nucleated. As the ejected catalyst moves outward in the plasma, the site where nucleation has taken place becomes directly exposed to the flow of carbon around the catalyst. At the C-Ni nucleation site, the uptake of carbon from the plasma is high. In this way, elongation of the tube becomes rapid. As the elongation of the nanotube proceeds, the catalyst particle on which the nanotube is growing reorientates to a position of least resistance as it moves away from the target. In doing this, the catalyst-nanotube would resemble a comet. Such an orientation will increase the rate at which C_2 is assimilated at the C–Ni interface and subsequent release of energy due to heat of formation.

Hence, nucleation and rapid initial growth takes place early in the plasma lifetime, i.e., between $0.5 - 2 \ \mu s$.

VI. CONCLUSION

In situ OES was used to characterize laser induced plasma plumes in the laser-furnace method used for synthesizing SWCNTs. The temporal and spatial behavior of the Swan band intensity of C_2 emissions at 516.5 nm were investigated. Spatial and temporal evolution of the electron density and electron temperature measurements were based on the emissions of singly charged CII ions. OES results were correlated with Raman spectroscopy. The temporal and spatial behavior of C_2 emissions were found to be sensitive to the variation in pressure and flow rate of argon gas. At low pressures the plasma plume expanded adiabatically and the C_2 intensity was found to decrease monotonically. During conditions which favored SWCNT synthesis, a sharp drop in C_2 emission was observed followed by a rise in emission intensity. The temporal and spatial behavior of the electron density under favorable conditions showed a rise in electron density at around 900 ns. Similarly, and only under favorable synthesis conditions, a sharp rise in electron temperature at approximately 900 ns was observed. From these OES observations and together with Raman measurements, it is concluded that the sharp drop in C_2 peak intensities and subsequent rise in electron densities and electron temperature was a direct consequence of the nucleation and rapid growth of SWCNTs on carbon-metal catalyst nanoparticles. The growth of a crystalline superstructure is exothermic and this released energy reheats the remaining plasma constituents. In conclusion we report experimental evidence for the role of C_2 in the early nucleation of SWCNTs and we demonstrate that OES is an excellent method to optimize the experimental conditions required for SWCNTs synthesis.

ACKNOWLEDGMENTS

[1]M. Dresselhaus, G. Dresselhaus, and A. Jorio, Phys. Rep. **409**, 47 (2005).

[2]A. P. Ramirez, Bell Lab. Tech. J. **10**, 171 (2005).

[3]M. Trojanowicz, Trends Analyt. Chem. **25**, 480 (2006).

[4]C. N. R. Rao and A. Cheetham, J. Mater. Chem. **11**, 2887 (2001).

[5]M. Arnold, A. A. Green, J. Hulvat, S. Stupp, and M. Hersam, Nat. Nanotechnol. **1**, 60 (2006).

[6]D. Bethune, C. Kiang, M. de Vries, G. Gorman, R. Savoy, J. Vazquez, and R. Beyers, Nature (London) **363**, 605 (1993).

[7]J. Kong, H. T. Soh, A. Cassell, C. F. Quate, and H. Dai, Nature (London) **395**, 878 (1998).

[8]T. Guo, P. Nikolaev, A. Thess, D. Colbert, and R. Smalley, Chem. Phys. Lett. **243**, 49 (1995).

[9]S. Arepalli, P. Nikolaev, W. Holmes, and C. Scott, Appl. Phys. A: Mater. Sci. Process. **69**, 1 (1999).

[10]S. Arepalli, P. Nikolaev, W. Holmes, and C. Scott, Appl. Phys. A: Mater. Sci. Process. **70**, 125 (2000).

[11]T. Ishigaki, S. Suzuki, H. Kataura, W. Kratschemer, and Y. Achiba, Appl. Phys. A: Mater. Sci. Process. **70**, 121 (2000).

[12]A. A. Puretzky, H. Schittenhelm, X. Fan, M. Lance, L. F. Allard, and D. B. Geohegan, Phys. Rev. B **65**, 245425 (2002).

[13]T. Ikegami, F. Nakanishi, M. Uchiyama, and K. Ebihara, Thin Solid Films **457**, 7 (2004).

[14]M. Nishio, S. Akita, and Y. Nakayama, Thin Solid Films **464–465**, 304 (2004).

[15]S. H. Lim, H. S. Yoon, J. H. Moon, K. C. Park, and J. Jang, Appl. Phys. Lett. **88**, 033114 (2006).

[16]Z. Marković, B. Todorović-Markovi, I. Mohai, Z. Ka'roly, J. Sze'pvoölgyi, and Z. Farkas, Fullerenes, Nanotubes, Carbon Nanostuct. **13**, 215 (2005).

[17]J. García-Céspedes, M. Rubio-Roy, M. C. Polo, E. Pascual, J. Andújar, and E. Bertran, Diamond Relat. Mater. **16**, 1131 (2007).

[18]R. K. Garg, T. N. Anderson, R. P. Lucht, T. S. Fisher, and J. P. Gore, J. Phys. D **41**, 095206 (2008).

[19]H. Griem, *Plasma Spectroscopy* (McGraw Hill, New York, 1964).

[20]A. Thorn, *Spectrophysics* (Chapman and Hall, London, 1974).

[21]G. Befki, *Principal of Laser Plasmas* (Wiley, New York, 1976).

[22]See supplementary material at 10.1063/1.3311563 for [give brief description of material].

[23]NIST http://physics.nist.gov/PhysRefData/ASD/linesform.html, for details on how certain calculated values reflected in the text main were determined.

[24]S. S. Harilal, C. Bindhu, R. Issac, V. Nampoori, and C. P. G. Vallabhan, J. Appl. Phys. **82**, 2140 (1997).

[25]W. Lochte-Holtgreven, in *Plasma Diagnostics*, edited by W. Lochte-Holtgreven (North Holland, Amsterdam, 1968).

[26]C. Aragón and J. A. Aguilera, Spectrochim. Acta, Part B **63**, 893 (2008).

[27]S. Reich, C. Thomsen, and J. Maultzsch, *Carbon Nanotubes: Basic Concepts and Physical Properties*, 1st ed. (Wiley-VCH Verlag GmbH, Weinheim, 2004), Vol. 1, Chap. 7, p. 115.

[28]J. Maultzsch, H. Telg, S. Reich, and C. Thomsen, Phys. Rev. B **72**, 205438 (2005).

[29]J. Maultzsch, S. Reich, C. Thomsen, S. Webster, R. Czerw, D. Caroll, S. Vieira, P. Birkett, and C. Rego, Appl. Phys. Lett. **81**, 2647 (2002).

[30]A. van Orden and R. Saykally, Chem. Rev. **98**, 2313 (2002).

[31]R. Saito, G. Dresselhaus, and M. S. Dresselhaus, J. Appl. Phys. **73**, 494 (1993).

[32]A. Maiti, C. J. Brabec, C. M. Roland, and J. Bernholc, Phys. Rev. Lett. **73**, 2468 (1994).

[33]F. Kokai, K. Takahashi, D. Kasuya, M. Yudasaka, and S. Iijima, Appl. Phys. A: Mater. Sci. Process. **73**, 401 (2001).

[34]F. Kokai, K. Takahashi, D. Kasuya, M. Yudasaka, and S. Iijima, Appl. Surf. Sci. **197–198**, 650 (2002).

[35]G. Radhakrishnan, P. Adams, and L. Bernstein, Appl. Surf. Sci. **253**, 7651 (2007).

[36]D. G. M. Marchand, C. Journet, J.-M. Benoit, B. I. Yakobson, and S. T. Purcell, Nano Lett. **9**, 2961 (2009).

[37]S. I. Y. Ohta, Y. Okamoto, and K. Morokuma, ACS Nano **2**, 1437 (2008).

[38]A. Ferrari, Diamond Relat. Mater. **11**, 1437 (2002).

[39]S. S. Harilal, R. C. Isaac, C. V. Bindhu, V. P. N. Nampoori, and C. P. G. Vallabhan, J. Appl. Phys. **81**, 3637 (1997).

[40]S. S. Harilal, R. C. Isaac, C. V. Bindhu, V. P. N. Nampoori, and C. P. G. Vallabhan, J. Appl. Phys. **80**, 3561 (1996).

[41]D. Pappas, K. Saenger, J. Cuomo, and R. Dreyfus, J. Appl. Phys. **72**, 3966 (1992).

[42] D. B. Geohegen, in *Pulsed Laser Deposition of Thin Films*, 1st ed., edited by D. B. Chrissy (Wiley, New York, 1994), Vol. 1, Chap. 5, p. 115.

[43] A. Gorbunoff and O. Jost, in *Pulsed laser deposition of thin films: Applications-led growth of functional materials*, 1st ed., edited by R. Eason (Wiley, New York, 2006), Vol. 1, Chap. 24, p. 613.

[44] A. Wiltner and C. Linsmeier, Phys. Status Solidi A **201**, 881 (2004).

[45] International Centre for Diffraction Data (ICDD): File (00–06–0697).

[46] M. Moodley, N. Coville, B. Holloway, and M. Maaza, S. Afr. J. Med. Sci. **102**, 364 (2006).

[47] D. Laplaze, L. Alvarez, T. Guillard, J. Badie, and G. Flamant, Carbon **40**, 1621 (2002).

[48] Y. Leng, L. Xie, F. Liao, J. Zheng, and X. Li, Thermochim. Acta **473**, 14 (2008).

[49] S. Esconjauregui, C. Whelan, and K. Maex, Carbon **47**, 659 (2009).

[50] X. Fan, R. Buczko, A. A. Puretzky, D. B. Geohegen, J. Howe, S. Pantelides, and S. J. Pennycook, Phys. Rev. Lett. **90**, 145501 (2003).

[51] S. Khan and S. Ahmad, Nanotechnology **17**, 4654 (2006).

[52] S. Lair, W. Herndon, L. Murr, and S. Quinones, Carbon **44**, 447 (2006).

[53] S. Lebedkin, P. Scheiss, B. Renker, S. Malik, F. Henrich, M. Neumaier, C. Stoermer, and M. Kappes, Carbon **40**, 417 (2002).

[54] J. Gavillet, A. Loiseau, F. Ducastelle, S. Thair, P. Bernier, O. Stephan, and J.-C. C. J. Thibault, Carbon **40**, 1649 (2002).